Nat Mater. Author manuscript; available in PMC 2016 June 07.

Published in final edited form as:
Nat Mater. 2016 February ; 15(2): 164–168. doi:10.1038/nmat4490.

The classical and quantum dynamics of molecular spins on graphene

Christian Cervetti[1,*], **Angelo Rettori**[2], **Maria Gloria Pini**[3], **Andrea Cornia**[4], **Ana Repollés**[5], **Fernando Luis**[5], **Martin Dressel**[1], **Stephan Rauschenbach**[6], **Klaus Kern**[6,7], **Marko Burghard**[6], and **Lapo Bogani**[1,8,*]

[1]1. Physikalisches Institut, Universität Stuttgart, Pfaffenwaldring 57, D-70550 Stuttgart (Germany) [2]Dipartimento di Fisica, Università di Firenze, Via G. Sansone 1, I-50019 Sesto Fiorentino (Italy) [3]Istituto dei Sistemi Complessi, CNR, Unità di Firenze, Via Madonna del Piano 10, I-50019 Sesto Fiorentino (Italy) [4]Dipartimento di Scienze Chimiche e Geologiche, Università di Modena e Reggio Emilia, INSTM RU, Via G. Campi 183, I-41125 Modena (Italy) [5]Instituto de Ciencia de Materiales de Aragón, CSIC-Universidad de Zaragoza, C/ Pedro Cerbuna 12, E-50009 Zaragoza (Spain) [6]Max-Planck-Institut für Festkörperforschung, Heisenbergstrasse 1, D-70569 Stuttgart (Germany) [7]Institut de Physique de la Matière Condensée, Ecole Polytechnique Fédérale de Lausanne (EPFL), CH-1015 Lausanne, (Switzerland) [8]Department of Materials, University of Oxford, 16 Parks Road, OX1 3PH Oxford, (United Kingdom)

Abstract

Controlling the dynamics of spins on surfaces is pivotal to the design of spintronic[1] and quantum computing[2] devices. Proposed schemes involve the interaction of spins with graphene to enable surface-state spintronics[3,4], and electrical spin-manipulation[4-11]. However, the influence of the graphene environment on the spin systems has yet to be unraveled[12]. Here we explore the spin-graphene interaction by studying the classical and quantum dynamics of molecular magnets[13] on graphene. While the static spin response remains unaltered, the quantum spin dynamics and associated selection rules are profoundly modulated. The couplings to graphene phonons, to other spins, and to Dirac fermions are quantified using a newly-developed model. Coupling to Dirac electrons introduces a dominant quantum-relaxation channel that, by driving the spins over Villain's threshold, gives rise to fully-coherent, resonant spin tunneling. Our findings provide fundamental insight into the interaction between spins and graphene, establishing the basis for electrical spin-manipulation in graphene nanodevices.

* lapo.bogani@materials.ox.ac.uk. * cervetti.christian@gmail.com.

Author contributions

C.C. performed the functionalization and most measurements. A.C. synthetized the molecules. C.C. and S.R. acquired the MALDI-TOF spectra. A.R. and F.L. performed the very-low-temperature magnetic measurements. A.R., M.G.P. and L.B. performed the theoretical analysis. L.B. and M.B. conceived the experiments. L.B. wrote the draft and all authors contributed to discussions and the final manuscript.

Additional information

The authors declare no competing financial interests.

Supplementary information (SI) accompanies this paper at www.nature.com.

Europe PMC Funders Author Manuscripts

Keywords

graphene; spin dynamics; nanomaterials; quantum tunneling; molecular magnetism

Carbon-based spintronics offers means to manipulate localized spins in close proximity of a carbon nanotube[14-16] or graphene sheet[4-11]. This task requires understanding and tuning the interaction between the components, in order to minimize quantum-decoherence[16], and to enable spin manipulation, e.g. by controlling either the magnetic anisotropy[18] or the electronic coupling[5,19]. Here, we exploit the exceptionally-clean magnetic features of single-molecule-magnets (SMMs)[13] to explore how spins interact with graphene substrates.

The graphene-SMM hybrids are obtained by non-covalent grafting of $[Fe_4(L)_2(dpm)_6]$, (Hdpm=dipivaloylmethane and H_3L=2-hydroxymethyl-2-(4-(pyren-1-yl)-butoxy)methylpropane-1,3-diol, Fig.1a)[20] via solution-based assembly onto exfoliated graphene sheets. The two pyrene groups serve as anchors[20] to the graphene sheet. Functionalization of both solid-supported and bulk dispersions of graphene layers (Methods) allows determining the aggregation behaviour of the molecules on surface and performing magnetization measurements on statistically-relevant samples.

Atomic force microscopy (AFM) confirms successful decoration of graphene by $[Fe_4(L)_2(dpm)_6]$ (Fig.1b). Similar coverage was observed for single- and multi-layer graphene. Sufficiently low concentrations of $[Fe_4(L)_2(dpm)_6]$ ($C<10^{-6}$ M) ensure decoration by individual molecules without appreciable aggregation, while a full layer is formed for $C>10^{-5}$ M (SI). Multiple techniques evidence that the deposited SMMs are structurally and electronically intact. In particular, the height distribution in AFM images peaks at 1.8±0.3 nm (Fig.1c), in close agreement with the size of a single $[Fe_4(L)_2(dpm)_6]$ molecule.[20] In addition, Raman spectra (Fig.1d) exhibit only a small up-shift of the graphene G-band by ~4 cm^{-1} after functionalization, indicating slight p-type doping[21]. This conclusion is supported by the small positive shift of the charge-neutrality-point observed in the resistance *vs.* gate voltage curves (Figs.1e and 1f), corresponding to a charge-transfer of only 0.08 e^- per SMM. Furthermore, X-ray photoelectron spectra display the same characteristic Fe_{2p} peak positions of thick films of $[Fe_4(L)_2(dpm)_6]$ (SI) and mass spectra evidence clear fingerprints of intact $[Fe_4(L)_2(dpm)_6]$ at 1919, 1763 and 1736 amu (Fig.1g and SI).

The static magnetic properties of the hybrids are indistinguishable from those of crystalline $[Fe_4(L)_2(dpm)_6]$ (Fig.2). The temperature (T) dependence of the $\chi_m T$ curves (where χ_m is the static molar magnetic susceptibility, defined as the ratio between magnetization and the applied magnetic field, M/H) displays the same minimum at 100 K and a maximum around 6 K (Fig.2a, SI). The M *vs* H data also match within experimental error. The characteristic $\chi_m T$ *vs* T curve can be fitted[20] by considering g=2.00±0.05 and two intramolecular exchange interactions between nearest-neighbour and next-nearest-neighbour Fe(III) ions (with exchange constants J_{NN}=14.85±0.05 cm^{-1} and J_{NNN}=0.09±0.05 cm^{-1}, respectively), in excellent agreement with previous investigations, confirming a total spin ground state S=5.

The low-temperature magnetic properties of SMMs are dominated by the presence of a large magnetic anisotropy[13], which partially lifts the degeneracy of the ground multiplet and creates an energy barrier ΔE separating the $|m_s\rangle$ and $|-m_s\rangle$ states (Fig.3a). Two spin-relaxation mechanisms are thus possible: a classical overbarrier process, where multiple phonon absorptions allow overcoming ΔE, and a quantum tunneling (QT) mechanism, which takes place between degenerate levels at opposite sides of the barrier[13]. QT can be suppressed by applying an external magnetic field H that lifts the degeneracy of the $|\pm m_s\rangle$ levels. This allows examining the effect of graphene on both relaxation mechanisms separately.

The magnetization dynamics is probed by measuring the real (χ') and imaginary (χ'') response to a small magnetic field oscillating at frequency ω. In a static field H=1 kOe (Fig. 3b), where only thermally-activated behaviour is present, isolated molecules on graphene show a faster magnetization dynamics than those in crystalline $[Fe_4(L)_2(dpm)_6]$, for which Arrhenius analysis yields a barrier ΔE=9.7±0.7 cm^{-1}. In H=0 (Fig.3c), all $|m_s\rangle$ and $|-m_s\rangle$ sublevels fall back into resonance and QT is activated, thereby magnifying enormously the differences between the hybrids and crystals response. The T-dependence of the spin relaxation time, τ, (Fig.4a) shows that for crystalline $[Fe_4(L)_2(dpm)_6]$ the thermally-activated region persists down to 800 mK, below which temperature QT sets in. This contrasts strikingly with the spin relaxation in the hybrids, which is entirely dominated by QT, and the QT-rate is about one million times higher (τ^{-1} =10^5 Hz vs. 10^{-1} Hz).

To explain these observations we subdivide the spin anisotropy into different contributions, with each term having the symmetry of a corresponding tesseral harmonic. This approach produces an intuitive but rigorous picture of the spin behaviour via the Hamiltonian:

$$\mathrm{H}=\mu_{\mathrm{B}} S g H+\sum_{\substack{i\geq 2\\ j\leq i}}^{2S} B_i^j \hat{O}_i^j \qquad (1)$$

where the first term describes the Zeeman interaction between the molecular spin S and H (μ_B is the Bohr magneton, g is the Landé factor) and the second models the spin anisotropy via the spin operators $\hat{O}_i^j$ that correspond to different harmonics, each weighted by a coefficient B_i^j. These operators, called Stevens operator-equivalents[13,22] contain the j^{th} power of the spin ladder operators, $\hat{S}_+$ and $\hat{S}_-$, and the $(i\text{-}j)^{\text{th}}$ power of $\hat{S}_z$ (see SI for explicit expressions and a pictorial representation of the associated harmonics). With equation (1) we can model the effect of any external electric field, e.g. the electron density of an underlying substrate, by introducing in the sum a term of corresponding symmetry[12,22] and discarding all terms not belonging to the point group of the spin environment. Stevens operator-equivalents have an effect on both classical and quantum relaxation channels: $\hat{O}_i^j$ terms with j=0 contain powers of $\hat{S}_z$ only, and contribute to ΔE but do not mix the $|m_s\rangle$ eigenstates; terms with $j\neq 0$, on the contrary, mix states differing in m_s by a multiple of j, opening the QT relaxation channel.

For crystalline $[Fe_4(L)_2(dpm)_6]$, equation (1) reads $H=B_2^0\hat{O}_2^0+B_2^2\hat{O}_2^2+B_4^0\hat{O}_4^0+B_4^3\hat{O}_4^3+\mu_B SgH$, and electron paramagnetic resonance (EPR) studies yield[20] $B_2^0=-0.136\pm0.003\ \mathrm{cm}^{-1}$, $B_2^2=8.1\pm0.7\cdot10^{-3}\ \mathrm{cm}^{-1}$, $B_4^0=2.4\pm0.5\cdot10^{-5}\ \mathrm{cm}^{-1}$ and g=2.000±0.005. Being B_2^0 the leading $\hat{J}$=0 term, $\Delta E\cong 3|B_2^0|S^2$, while multiple spectroscopic and magnetic investigations on related systems determined B_4^3 to be <5±1·10^{-4} cm^{-1}. By using g=2.004±0.003 and $B_2^0=-0.12\pm0.02\ \mathrm{cm}^{-1}$, the magnetization curves of both hybrids and crystals (Fig.2b) are perfectly reproduced. Moreover, the barrier value extracted from the dynamics provide $B_2^0=-0.13\pm0.01\ \mathrm{cm}^{-1}$, again leading to an excellent overall agreement for the leading anisotropy term. Axial distortion of the SMMs on graphene can thus be excluded.

We now discuss how the graphene environment alters the spin-relaxation (Fig.4b). Dipolar and hyperfine interactions introduce a local dynamic magnetic field distribution that alters the QT rate by broadening the QT resonances[13,25] (Fig.3a). The widths of these distributions, as determined[25,26] from dilution and nuclear resonance experiments in crystals, are ~200 and 1 Oe, respectively. In the hybrids, intermolecular dipolar interactions are strongly reduced due to the sizeable separation between the molecules and magnetic shielding by graphene, which is predicted to be extremely efficient[27]. On the contrary, hyperfine interactions arise from the nuclei inside the molecules themselves, and are unaffected by the substrate. Overall, this imposes an intrinsic upper limit of ~10 Hz to the QT-rate of isolated $[Fe_4(L)_2(dpm)_6]$ (Fig.4a).[13,25,26] Any additional acceleration of QT must arise from interaction with the graphene layer.

To evaluate the effect of graphene vibrations, we extend the established theoretical framework[23,24] to two-dimensional phonon baths (SI). In principle, the effect of phonons on each molecular group is to induce a time-dependent modification (or “modulation”) of any term of the magnetic energy. However, it can be shown[13] that, at low temperatures, the modulation of the isotropic exchange does not induce transitions between the $|m_s\rangle$ sublevels of the lowest exchange multiplet. Therefore, as we are interested in temperatures much lower than the Debye temperature, the only significant contribution will arise from the modulation of the anisotropy energy induced by long-wavelength acoustic phonons. The transition probabilities can be obtained[23,24] by adding to equation (1) the spin-phonon perturbation term $H_{SP}=i\sum_{q,\lambda}\sqrt{\frac{\hbar}{2m_c\omega_{q,\lambda}}}V_{q,\lambda}(\mathbf{S})\left(C_{q,\lambda}-C_{q,\lambda}^{\dagger}\right)$, where ω, q and λ are the phonon frequency, wavevector and polarization, $\hbar$ the Planck constant, m_c the unit cell mass, $V_{q,\lambda}$ the spin-phonon interaction potential, $C_{q,\lambda}$ the phonon creation operator, with the sum running over the Brillouin zone. For intact molecules, similar local distortions are expected in both crystals and hybrids and, provided that B_2^0 is essentially unaltered, as in the present case, $V_{q,\lambda}$ will also be similar in both materials. On the contrary, the different phonon densities of three- and two-dimensional baths will strongly alter the relaxation dynamics. For the hybrids, the relevant phonon bath can be described by the long-wavelength spectrum of the acoustic branches of graphene, which has an analytical expression[21]. Under these assumptions we obtain (see SI) the following relation:

$$\frac{R_c}{R_h}=\frac{2}{3}\frac{\rho_h \mathrm{k_B}}{\rho_c \pi \hbar}\frac{C_h^4}{C_c^5} \quad (2)$$

where *c* and *h* subscripts denote crystals and hybrids, *R* is a parameter proportional to the experimentally-observable phonon-induced relaxation rate, ρ the mass density, *C* the sound velocity and k_B is Boltzmann constant. This model provides excellent agreement with the data at $H\neq0$, where the relaxation is expected to be dominated by spin-phonon interactions (Fig.3b), simultaneously accounting for the behaviour in both crystals and hybrids. Notably, no fitting parameters are necessary, and full, quantitative agreement is attained by using the same set of B_i^j coefficients and introducing the known speed of sound of graphene[21], $C_h = 2{\cdot}10^4$ m/s, for the hybrids. It is noteworthy that the behaviour of crystalline $[Fe_4(L)_2(dpm)_6]$ is restored in hybrids with large SMM aggregates, for which the vibrational bath more closely resembles the three dimensional case (SI). These observations underscore the relevance of graphene vibrational modes for classical spin relaxation.

By contrast, the different phonon bath cannot explain the striking enhancement of QT at $H=0$ (Fig.4a), which requires introducing the coupling to graphene electrons. The latter is expressed, within Stevens' formalism[13,22], by including the perturbation integral $\langle m_s(\psi_M)|V_I|\psi_G\rangle$, where molecular and graphene electronic states (ψ_M and ψ_G, respectively) interact via the potential V_I, altering the $\langle m_s|$ spin state. The wavefunction ψ_G has threefold symmetry, and the corresponding point-group[22] permits non-vanishing integral terms only for B_i^j coefficients with *j* a multiple of 3, independently of the form of V_I. In the perturbation treatment of the spin-graphene interaction, all such terms have an identical effect on the level mixing and the QT rate of the lowest $|m_s\rangle$ levels, differing only in the perturbation order. To address QT, we merge all terms into an effective overall graphene effect represented by the leading-order term $B_4^3\hat{O}_4^3=B_4^3\left\lfloor \hat{S}_z\left(\hat{S}_+^3+\hat{S}_-^3\right)+\left(\hat{S}_+^3+\hat{S}_-^3\right)\hat{S}_z\right\rfloor/4$, which directly admixes only the $m_s=\pm3$ states (direct mixing of lower levels would require lower symmetry terms, such as $B_2^2\hat{O}_2^2$). By introducing a $B_4^3>2\cdot10^{-3}\ \mathrm{cm}^{-1}$ term into the simulations, while maintaining all other parameters, both the ac-susceptibility peak (Fig.3c) and the *T*-dependence of τ (Fig.4a) are excellently reproduced. A pictorial representation of the spin anisotropy in the crystals and hybrids (Fig.4c) highlights the significant weight of the additional $\hat{O}_4^3$ term and the signature of the threefold rotational symmetry of graphene on the spin anisotropy. The explicit operator form of the microscopic interaction potential V_I is debated. One possibility is the Heisenberg form $\hat{\Xi}=\left(\hat{S}_+\hat{\sigma}_-+\hat{S}_-\hat{\sigma}_++2\hat{S}_z\hat{\sigma}_z\right)/2$, where $\hat{\sigma}_+$, $\hat{\sigma}_-$, $\hat{\sigma}_z$ are the spin operators of the Dirac-fermion, nevertheless the nature of the underlying scattering processes remains debated. For $[Fe_4(L)_2(dpm)_6]$, a direct quantitative comparison among the different proposals is intricate, because of the cumbersome *ab initio* evaluation of the amplitude cross-sections. Most importantly, spin-flip processes as efficient as observed for the hybrids are only predicted when scattering due to the presence of two K points is included in the theory[28], and the values here obtained can be used to validate the theoretical models proposed for spin-Dirac fermion interactions[29].

Strongly-perturbative QT of spins, predicted by Villain decades ago[13], strictly requires pronounced electronic perturbations combined with minimal dipolar interactions. These conditions are hard to fulfil in crystals, such that the quantum spin dynamics of Villain's regime has so far eluded observation. Graphene hybrids offer the ideal conditions by simultaneously suppressing dipolar interactions and electronically enhancing the transverse anisotropy terms. For suppressed dipolar fields, weak perturbations (as in crystals) lead to a non-monotonic behaviour in the τ vs T plot, where standard tunnelling is followed by a slow descent into Villain's QT regime (SI). In contrast, the B_4^3 perturbation term introduced by graphene is large enough to directly drive the spins into Villain's regime (Fig.4d), leading to a monotonous temperature dependence of τ. The associated threshold yields a lower bound of 0.3 μeV for the interaction between SMM spins and the Dirac electrons, lower than the estimated spin-orbit coupling in graphene.

To conclude, our observations set the theoretical and experimental basis for the exploration of the magnetic effects introduced by localized spins in graphene. The clear roles of the vibrational and electronic interactions, here unravelled, can now be exploited in the design of spin-nanomechanical and nanospintronic devices. The strong graphene-induced terms allows envisaging coherent electric spin manipulation, via electrically-tuned spin mixing, allowing molecular spin control in ways hitherto reserved to other qubits[30]. The observed interaction already introduces a spin-level mixing comparable to those used for qubit manipulations[30], and the use of molecular magnets with even higher spin-orbit coupling (e.g. rare-earths) could enhance such effects even further. Similar effects, with the same symmetry, can also be envisaged for other systems, e.g. SMMs on reconstructed Au surfaces.[19] Villain's tunneling regime, being by definition coherent, opens also novel perspectives for quantum operations. Eventually, the observation of substrate effects on the quantum dynamics constitutes an important methodological tool, which can be applied to study other spin-substrate interactions, providing unique details on symmetry-breaking quantum effects.

Methods

$[Fe_4(L)_2(dpm)_6]$ was synthesized as previously reported[20]. Graphene was mechanically exfoliated from highly-oriented pyrolytic graphite onto Si/SiO_2 substrates. Surface hybrids were obtained by immersion in a solution of $[Fe_4(L)_2(dpm)_6]$ in 1,2-dichloroethane:dichloromethane (9/1, v/v) at room temperature, followed by washing with isopropanol. Bulk samples of the hybrids were prepared by first sonicating 8.4 mg of graphite powder in 20 ml of the solvent mixture for 48 hrs, followed by adding 11.5 mg of $[Fe_4(L)_2(dpm)_6]$ in 20 ml of the same mixture, followed by stirring for 45 min and final filtering through PTFE membranes (0.2 μm pore size). Magnetic measurements were corrected for the diamagnetism of the sample and sample holder, as independently determined. A home-built micro-SQUID susceptometer inside a dilution refrigerator was used for zero-field measurements, with extremely small ac field amplitudes (50 mOe) and the data corrected by the bare graphene signal. AFM images were acquired with a Bruker Icon system in tapping mode, using Olympus AC200TS cantilevers. MALDI-TOF spectra were recorded using a laser pulsed at ~4 Hz, while the XPS spectra were obtained with a

monochromatized Al-Kα source (1486.6 eV), see SI for details. Electronic devices were fabricated using a PMMA resist, e-beam lithography and thermally evaporated Au/Ti.

Supplementary Material

Refer to Web version on PubMed Central for supplementary material.

Acknowledgments

We thank J. Wrachtrup and E. Rastelli for discussions, M. Konuma, U. Stützel, J. Sesé, A. L. Barra, D. Drung, Th. Schurig and L. Sebeke for assistance with the measurements and financial support from Italian MIUR, Spanish MINECO (MAT2012-38318-C03-01), BW-Stiftung (Kompetenznetz Funktionelle Nanostrukturen), ERC-StG-338258 “OptoQMol”, the Royal Society (URF fellowship and grant) and the AvH Stiftung (Sofja Kovalevskaja award).

References

1. Sanvito S. Organic spintronics: Filtering spins with molecules. Nature Mater. 2011; 10:484–485. [PubMed: 21697848]
2. DiVincenzo DP. Quantum computation. Science. 1995; 270:255–261.
3. Pesin D, MacDonald AH. Spintronics and pseudospintronics in graphene and topological insulators. Nature Mater. 2012; 11:409–416. [PubMed: 22522641]
4. Han W, Kawakami RK, Gmitra M, Fabian M. Graphene spintronics. Nature Nano. 2014; 9:794–807.
5. Garnica M, et al. Long-range magnetic order in a purely organic 2D layer adsorbed on epitaxial graphene. Nature Phys. 2013; 9:368–374.
6. Nair RR, et al. Dual origin of defect magnetism in graphene and its reversible switching by molecular doping. Nature Comm. 2010; 4 DOI: 10.1038/ncomms3010.
7. Chen JJ-H, Li L, Cullen WGW, Williams EDE, Fuhrer MS. Tunable Kondo effect in graphene with defects. Nature Phys. 2011; 7:535–538.
8. Nair RR, et al. Spin-half paramagnetism in graphene induced by point defects. Nature Phys. 2012; 8:199–202.
9. Tombros N, Jozsa C, Popinciuc M, Jonkman HT, van Wees BJ. Electronic spin transport and spin precession in single graphene layers at room temperature. Nature. 2007; 448:571–574. [PubMed: 17632544]
10. McCreary KM, Swartz AG, Han W, Fabian J, Kawakami RJ. Magnetic Moment Formation in Graphene Detected by Scattering of Pure Spin Currents. Phys. Rev. Lett. 2012; 109:186604. [PubMed: 23215308]
11. Dlubak B, et al. A. Highly efficient spin transport in epitaxial graphene on SiC. Nature Phys. 2012; 8:557.
12. Cervetti C, Heintze E, Bogani L. Interweaving spins with their environment: novel inorganic nanohybrids with controllable magnetic properties. Dalton Trans. 2014; 43:4220–32. [PubMed: 24514949]
13. Gatteschi, D.; Sessoli, R.; Villain, J. Molecular Nanomagnets. Oxford University Press; Oxford: 2006.
14. Hueso LE, et al. Transformation of spin information into large electrical signals using carbon nanotubes. Nature. 2007; 445:410–413. [PubMed: 17251975]
15. Laird EA, Pei F, Kouwenhoven LP. A valley-spin qubit in a carbon nanotube. Nature Nano. 2013; 8:565–568.
16. Kuemmeth F, Ilani S, Ralph DC, McEuen PL. Coupling of Spin and Orbital Motion of Electrons in Carbon Nanotubes. Nature. 2008; 452:448–452. [PubMed: 18368113]
17. Warner M, et al. Potential for spin-based information processing in a thin-film molecular semiconductor. Nature. 2013; 503:504–508. [PubMed: 24162849]

18. Oberg JC, Calvo MR, Delgado F, Moro-Lagare M, Serrante D, Jacob D, Fernández-Rossier J, Hirjibeddin CF. Control of single-spin magnetic anisotropy by exchange coupling. Nature Nano. 2014; 9:64–68.
19. Mannini M, et al. Quantum tunneling of the magnetization in a monolayer of oriented single-molecule magnets. Nature. 2010; 468:417–421. [PubMed: 20981008]
20. Bogani L, Danieli C, Biavardi E, Bendiab N, Barra AL, Dalcanale E, Wernsdorfer W, Cornia A. Single-molecule-magnets carbon-nanotube hybrids. Angew. Chem. Int. Ed. 2009; 121:760–764.
21. Ferrari AC, Basko DM. Raman spectroscopy as a versatile tool for studying the properties of graphene. Nature Nano. 2013; 8:235–246.
22. Misra SK, Poole CP, Farach HA. A review of spin Hamiltonian forms for various point-group site symmetries. Appl. Magn. Reson. 1996; 11:29–46.
23. Fort A, Rettori A, Villain J, Gatteschi D, Sessoli R. Mixed Quantum-Thermal Relaxation in Mn_{12} Acetate Molecules. Phys. Rev. Lett. 1998; 80:612–615.
24. Leuenberger MN, Loss D. Spin tunneling and phonon-assisted relaxation in Mn_{12}-acetate. Phys. Rev. B. 2000; 61:1286–1302.
25. Verniani L, Barra AL, Naugebauer P, Rodriguez-Douton MJ, Sessoli R, Sorace L, Wernsdorfer W, Cornia A. Magnetic bistability of isolated giant-spin centers in a diamagnetic crystalline matrix. Chem. Eur. J. 2012; 18:3390–3398. [PubMed: 22311823]
26. Repollés A, Cornia A, Luis F. Spin-lattice relaxation via quantum tunneling in diluted crystals of Fe_4 single-molecule magnets. Phys. Rev. B. 2014; 89:054429.
27. Koshino M, Arimura Y, Ando T. Magnetic field screening and mirroring in graphene. Phys. Rev. Lett. 2009; 102:177203. [PubMed: 19518822]
28. Trauzettel B, Bulaev DV, Loss D, Burkard G. Spin qubits in graphene quantum dots. Nat. Phys. 2007; 3:192–196.
29. Lundberg MB, Yang R, Renard J, Folk JA. Defect-mediated spin relaxation and dephasing in graphene. Phys. Rev. Lett. 2013; 110:156601. [PubMed: 25167293]
30. Yamamoto M, Takada S, Bäuerle C, Watanabe K, Wieck AD, Tarucha S. Electrical control of a solid-state flying qubit. Nature Nano. 2012; 7:247.

Europe PMC Funders Author Manuscripts

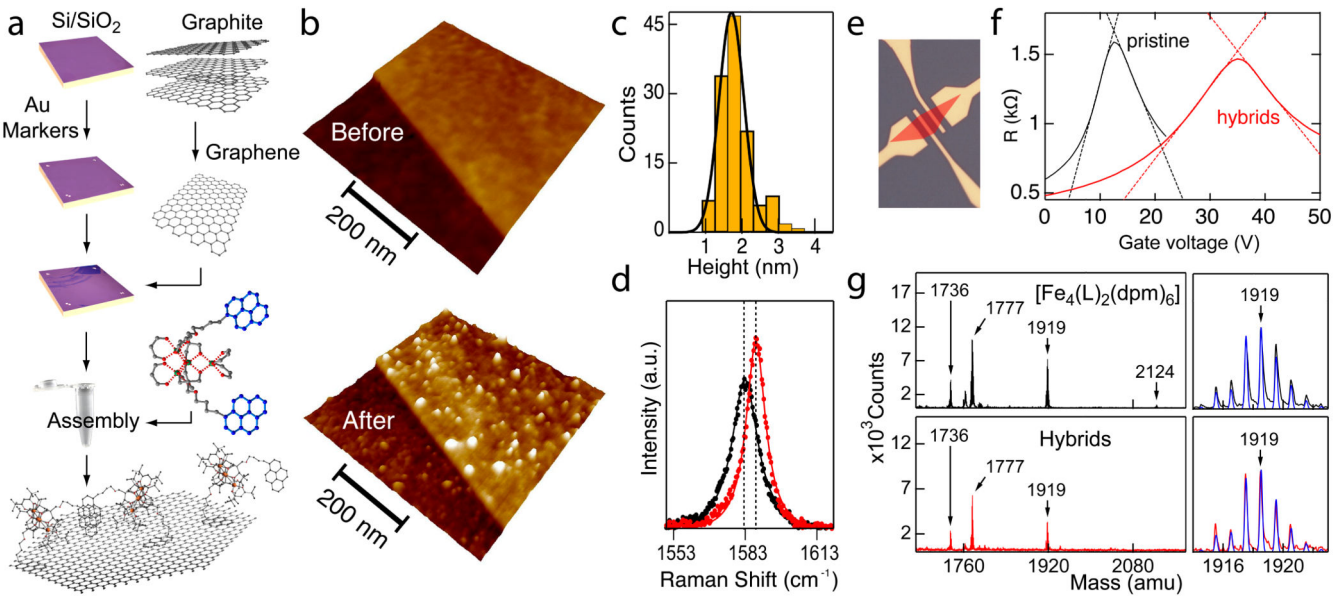

Figure 1. The graphene-spin hybrids

a) Grafting of the molecular magnets on graphene and crystal structure of $[Fe_4(L)_2(dpm)_6]$ (pyrene groups highlighted in blue, hydrogens and t-butyl groups omitted). b) AFM images of graphene flakes before and after grafting, at C=2.5·10^{-8} M. c) AFM height distribution for sub-monolayer coverage and Gaussian fitting, indicating a mean value of 1.8 nm. d) Raman G band, acquired with a 632.8 nm laser at the centre of an exfoliated graphene flake, before (black) and after (red) functionalization. Lines are fits to the data with single Lorentzian curves. e) Optical image of the graphene device, with the graphene flake outlined in red. f) Gate dependence of the four-terminal resistance for a single-flake graphene field-effect transistor, for pristine graphene (black) and after grafting (red), at C=10^{-4} M. Dashed lines highlight the region of constant charge carrier mobility. g) MALDI-TOF spectra of crystalline $[Fe_4(L)_2(dpm)_6]$ (top) and of the hybrids (bottom), and zoom-in on one isotropic pattern. Blue lines are simulations for intact cluster cores.

Europe PMC Funders Author Manuscripts

Europe PMC Funders Author Manuscripts

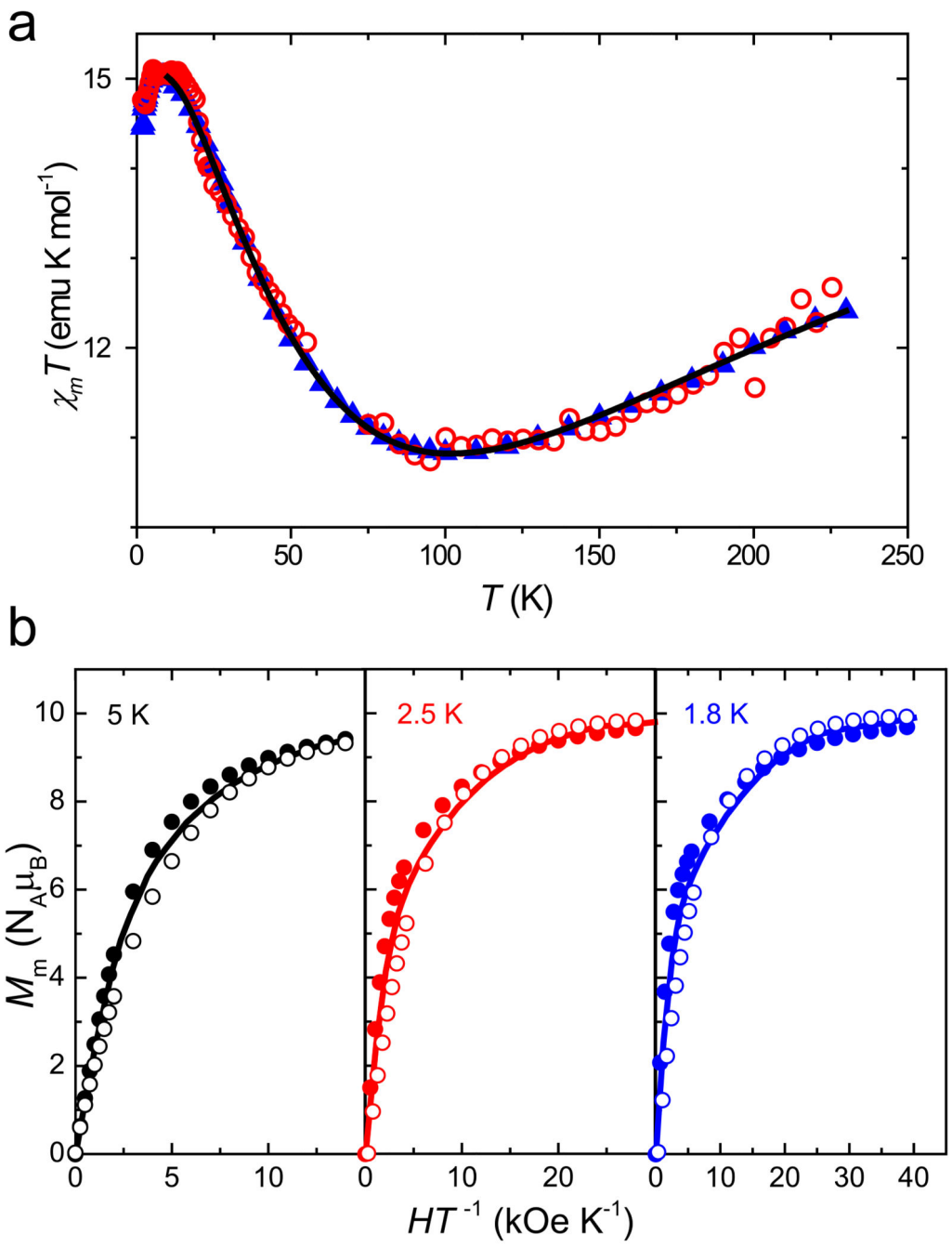

Figure 2. Static magnetic properties of the hybrids

a) Temperature dependence of the $\chi_m T$ product of for $[Fe_4(L)_2(dpm)_6]$[20] (triangles) and the hybrids (circles) (measured in H=1 kOe for the hybrids and H=1 kOe below 30 K and in 10 kOe above for the crystals). The black line represents fitting by considering the intact $[Fe_4(L)_2(dpm)_6]$ core (see text and Ref. 20). b) Comparison of the low-temperature magnetization curves of crystalline $[Fe_4(L)_2(dpm)_6]$ (solid points) and the graphene hybrids (open dots), showing the M_m vs H/T curves acquired at 5 K (left), 2.5 K (middle) and 1.8 K

(right) after subtracting the graphene matrix contribution and rescaling by the number of $[Fe_4(L)_2(dpm)_6]$ molecules. Solid lines are fits to the data (see text and Ref. 20).

Europe PMC Funders Author Manuscripts

Europe PMC Funders Author Manuscripts

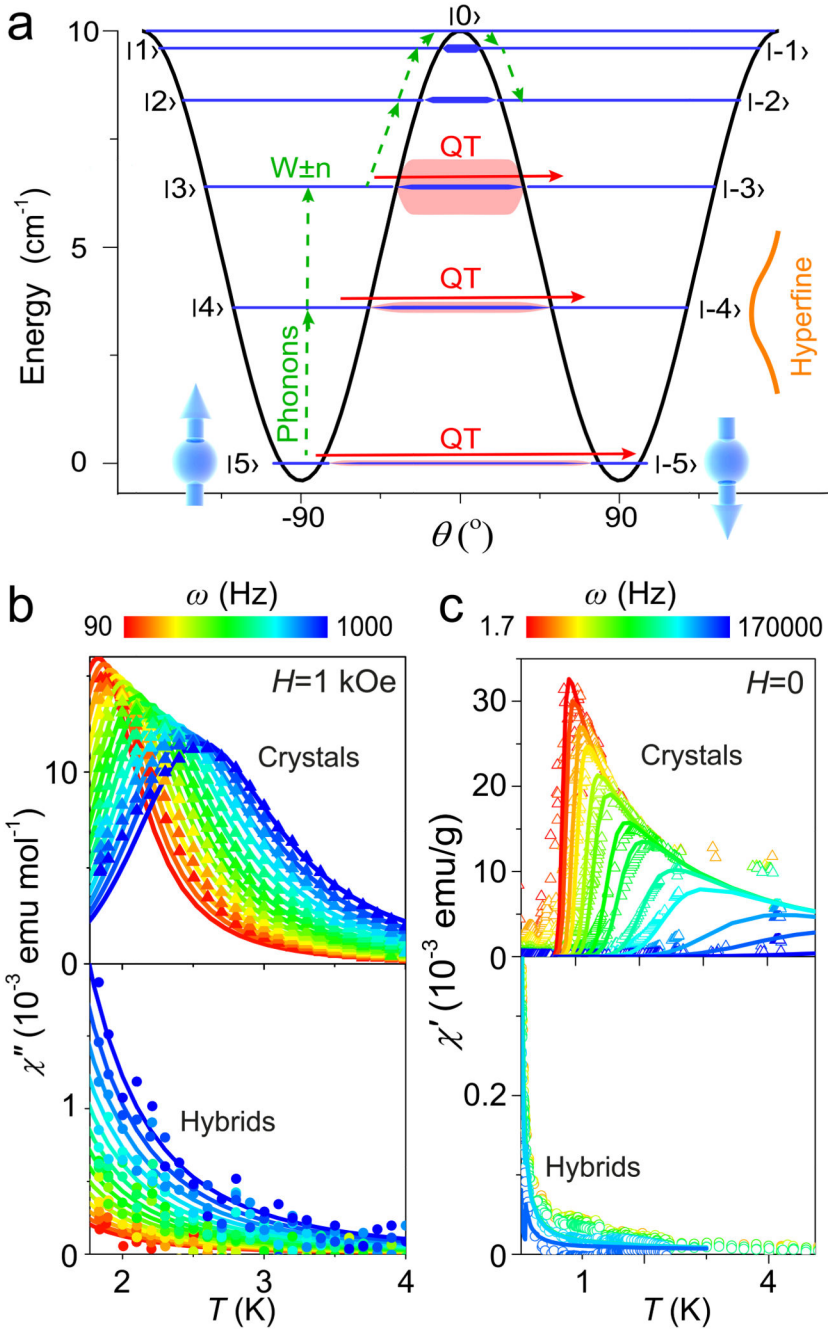

Figure 3. Classical and quantum magnetization dynamics

a) $|m_s\rangle$ sublevels of the ground state of the single-molecule-magnet $[Fe_4(L)_2(dpm)_6]$, as obtained from equation (1). Phonons determine transition probabilities (green arrows) to thermally overcome the barrier. Quantum tunneling happens between admixed levels (red arrows), while hyperfine and dipolar interactions create energy distributions (orange). Interaction with Dirac electrons increases the tunnel splittings below $|3\rangle$ and $|-3\rangle$ (red areas, exaggerated for clarity). b) Temperature and frequency dependence of the imaginary component of the dynamic susceptibility (χ'') in a magnetic field H=1 kOe for

$[Fe_4(L)_2(dpm)_6]$ (top) and hybrids with isolated molecules (bottom). Lines are simulations with the theory (see text for the theory). c) Temperature and frequency dependence of the real component of the dynamic susceptibility (χ') in H=0 for $[Fe_4(L)_2(dpm)_6]$ (top) and hybrids with isolated molecules (bottom). Lines are simulations with the theory (see text for the theory).

Europe PMC Funders Author Manuscripts

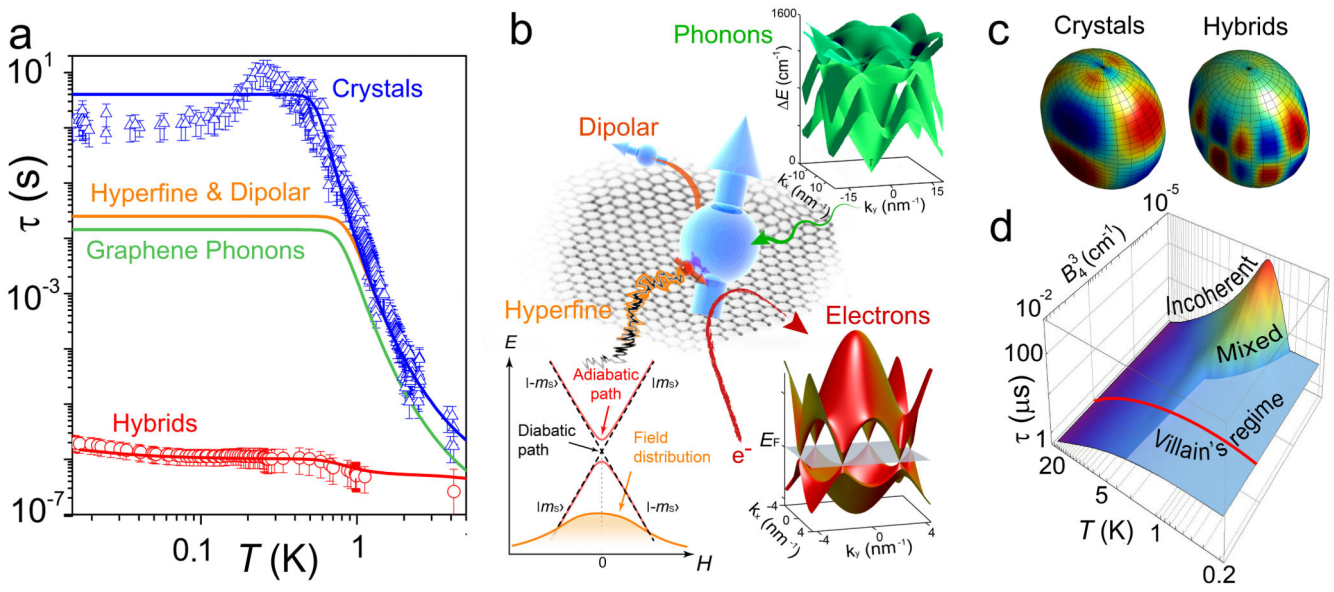

Figure 4. Contributions to the zero-field spin dynamics

a) Temperature dependence of the spin relaxation time in H=0, for $[Fe_4(L)_2(dpm)_6]$ (blue) and the hybrids (red). Lines show the curves for 0.3 Hz tunneling frequency, and the estimations of suppressed dipolar interactions (orange), graphene phonons (green) and Dirac electrons-spin interactions (red). b) Different contributions to relaxation lifetime of spins on graphene: The dipolar and hyperfine interactions produce dynamic field distributions around all avoided level crossings (orange); transition probabilities are determined by the graphene phonon dispersion (green surface); Dirac electrons (red surface) introduce quantum mixing terms with fingerprint symmetry. c) Representation of the resulting magnetic anisotropy for $[Fe_4(L)_2(dpm)_6]$ and the hybrids, visualizing the $B_4^3\hat{O}_4^3$ term arising from interactions with Dirac electrons. B_2^0 is decreased tenfold for clarity. d) Different tunneling regimes, as a function of temperature and of the strength of the perturbative driving term B_4^3. The regime of the experimentally-observed for the hybrids is highlighted in red.

Europe PMC Funders Author Manuscripts